



Article

Design of a Penta-Band Graphene-Based Terahertz Metamaterial Absorber with Fine Sensing Performance

Runing Lai ^{1,†}, Hao Chen ^{1,†}, Zigang Zhou ¹, Zao Yi ^{1,2,*} , Bin Tang ³ , Jing Chen ⁴ , Yougen Yi ⁵, Chaojun Tang ⁶, Jianguo Zhang ⁷ and Tangyou Sun ^{8,*}

¹ Joint Laboratory for Extreme Conditions Matter Properties, Tianfu Institute of Research and Innovation, State Key Laboratory of Environmental Friendly Energy Materials, Key Laboratory of Manufacturing Process Testing Technology of Ministry of Education, Southwest University of Science and Technology, Mianyang 621010, China; lrn3167160774@163.com (R.L.); chenhaoswustedu@163.com (H.C.); zhousigang1973@163.com (Z.Z.)

² School of Chemistry and Chemical Engineering, Jishou University, Jishou 416000, China

³ School of Microelectronics and Control Engineering, Changzhou University, Changzhou 213164, China; btang@cczu.edu.cn

⁴ College of Electronic and Optical Engineering, Nanjing University of Posts and Telecommunications, Nanjing 210023, China; jchen@njupt.edu.cn

⁵ College of Physics and Electronics, Central South University, Changsha 410083, China; yougenyi@csu.edu.cn

⁶ College of Science, Zhejiang University of Technology, Hangzhou 310023, China; chaojuntang@126.com

⁷ Department of Physics, Jinzhong University, Jinzhong 030619, China; phys.zhangjg@gmail.com

⁸ Guangxi Key Laboratory of Precision Navigation Technology and Application, Guilin University of Electronic Technology, Guilin 541004, China

* Correspondence: yizaomy@swust.edu.cn (Z.Y.); suntangyou@guet.edu.cn (T.S.); Tel./Fax: +86-0816-2480830 (Z.Y.); +86-0773-2290083 (T.S.)

† These authors contributed equally to this work.

Abstract: This paper presents a new theoretical proposal for a surface plasmon resonance (SPR) terahertz metamaterial absorber with five narrow absorption peaks. The overall structure comprises a sandwich stack consisting of a gold bottom layer, a silica medium, and a single-layer patterned graphene array on top. COMSOL simulation represents that the five absorption peaks under TE polarization are at $f_I = 1.99$ THz (95.82%), $f_{II} = 6.00$ THz (98.47%), $f_{III} = 7.37$ THz (98.72%), $f_{IV} = 8.47$ THz (99.87%), and $f_V = 9.38$ THz (97.20%), respectively, which is almost consistent with the absorption performance under TM polarization. In contrast to noble metal absorbers, its absorption rates and resonance frequencies can be dynamically regulated by controlling the Fermi level and relaxation time of graphene. In addition, the device can maintain high absorptivity at $0\sim 50^\circ$ in TE polarization and $0\sim 40^\circ$ in TM polarization. The maximum refractive index sensitivity can reach $S_V = 1.75$ THz/RIU, and the maximum figure of merit (FOM) can reach $FOM_V = 12.774$ RIU⁻¹. In conclusion, our design has the properties of dynamic tunability, polarization independence, wide-incident-angle absorption, and fine refractive index sensitivity. We believe that the device has potential applications in photodetectors, active optoelectronic devices, sensors, and other related fields.

Keywords: terahertz; graphene; penta-band absorption; dynamic tunability; wide-angle absorption; high figure of merit



Citation: Lai, R.; Chen, H.; Zhou, Z.; Yi, Z.; Tang, B.; Chen, J.; Yi, Y.; Tang, C.; Zhang, J.; Sun, T. Design of a Penta-Band Graphene-Based Terahertz Metamaterial Absorber with Fine Sensing Performance. *Micromachines* **2023**, *14*, 1802. <https://doi.org/10.3390/mi14091802>

Academic Editor: Andrey V. Novitsky

Received: 20 August 2023

Revised: 13 September 2023

Accepted: 19 September 2023

Published: 21 September 2023



Copyright: © 2023 by the authors. Licensee MDPI, Basel, Switzerland. This article is an open access article distributed under the terms and conditions of the Creative Commons Attribution (CC BY) license (<https://creativecommons.org/licenses/by/4.0/>).

1. Introduction

Terahertz (THz) waves constitute a distinctive subset within the electromagnetic spectrum, spanning a frequency range of 0.1~10 THz (1 THz = 10¹² Hz). This exceptional frequency band holds paramount significance across diverse domains, encompassing optical sensing [1], communication technology [2], biodetection [3], and optical stealth [4]. Its appeal emanates from its notable attributes, including low energy consumption [5], profound penetrability [6], and other commendable characteristics [7–9]. In practical applications, the meticulous regulation of terahertz wave parameters stands as an imperative

pursuit. Among these parameters, the amplitude modulation of terahertz waves utilizing surface plasmon resonance (SPR) metamaterial absorbers constitutes an inherently captivating research realm [10–12]. In various fields such as biochemical identification, environmental toxin detection, and safety assessment, the resonant frequencies of most biological molecules fall within the THz range, making THz absorbers more sensitive. They can provide detailed information about the structure and dynamic behavior of biological molecules, such as proteins, DNA, and cell membranes. In contrast, the frequency range of visible-light absorbers and infrared absorbers cannot achieve the sensitivity of the THz range. Moreover, THz absorbers operate at lower frequencies, which can prevent background and substrate absorption [13]. Furthermore, THz waves exhibit strong penetration capabilities, allowing them to penetrate many non-metallic and non-aqueous biological samples, such as cells and tissues. This enables non-destructive biological detection in the THz range, without the need for special sample treatment or the addition of labeling substances, avoiding detrimental effects on biological samples. Visible-light absorbers and infrared absorbers, due to their shorter wavelengths, have poorer penetration capabilities and typically require sample processing or the use of microscopy equipment for detection. Additionally, THz radiation has no significant damaging effects on biological systems, as it has low radiation energy and high biological safety. In contrast, visible-light absorbers and infrared absorbers may cause thermal damage or chemical reactions in biological systems under high-energy radiation. In summary, THz absorbers have a higher sensitivity, a wider range of applications, and greater potential compared to visible-light and infrared absorbers [14–16].

However, conventional configurations of metamaterial absorbers are beset by inherent constraints. Once established, adaptability becomes a challenge. For example, some notable references on the subject include metal absorbers [17,18], anisotropic plasmonic metasurfaces [19], and lithography-free metasurface absorbers [20]. Fixed absorptivity and resonance frequencies, accompanied by polarization dependencies and susceptibility to incident angles, collectively confine their pragmatic versatility. Hence, there is a compelling quest for a metamaterial absorber design capable of realizing tunable absorption performance, polarization independence, resistance to variations in incident angles, and exceptional sensing capabilities. In the pursuit of these goals, researchers have harnessed an array of diverse metamaterials, encompassing noble metals [21], graphene [22], vanadium dioxide [23], and Dirac semimetals [24]. Notably, graphene has risen to prominence as a standout candidate, owing to its unparalleled electrical conductivity and carrier mobility [25]. This material engenders swift spectral responses spanning the entire terahertz spectrum [26]. Employing geometric patterning, it incites robust localized surface plasmon resonance (LSPR) [27], enabling the achievement of multiple super-absorption bands and heightened absorption rates. Further enhancing its potential, the dynamic manipulation of graphene's Fermi energy level through applied voltage facilitates real-time adjustments to the device's absorption frequency and absorbance characteristics [28,29]. This distinctive capability empowers graphene-based SPR metamaterial absorbers to achieve impeccable absorption at chosen resonant frequencies. This confluence of exceptional attributes positions graphene-based SPR metamaterial absorbers as highly promising contenders for catalyzing pioneering advancements in the manipulation and absorption of terahertz waves.

As for the field of narrowband graphene-based SPR metamaterial absorbers, numerous designs have been reported. For instance, in 2019, Yan et al., explored the impact of Fermi level variation on resonance frequency in a tunable single-mode absorber, achieving an absorption rate of up to 99.99% at a Fermi level of 0 eV [30]. In 2022, Zhu et al., devised an absorber exhibiting both single-band and dual-band absorption characteristics: a 99.30% absorption rate was achieved at 16.0 THz; a 94.56% dual-band absorption rate was observed at 11.4 THz; and a 99.11% absorption rate occurred at 26.2 THz [31]. In 2023, Lai et al., reported a tripe-band SPR metamaterial absorber based on open-ended prohibited sign type mono-layer graphene, achieving three absorption peaks at 4.04 THz, 6.76 THz, and 9.40 THz [32]. Nonetheless, the majority of research has primarily concentrated on one to

three absorption peaks in graphene SPR metamaterial absorbers. There remains a scarcity of research reports concerning four or more absorption bands.

In this study, a novel THz graphene-based SPR metamaterial absorber is introduced. Numerical simulations reveal the emergence of penta-band absorption peaks under TE polarization at the frequencies $f_I = 1.99$ THz (95.82%), $f_{II} = 6.00$ THz (98.47%), $f_{III} = 7.37$ THz (98.72%), $f_{IV} = 8.47$ THz (99.87%), and $f_V = 9.38$ THz (97.20%). This absorption closely aligns with that observed under TM polarization. Subsequently, a detailed analysis of the absorptivity mechanism is carried out, employing transmission line theory and the equivalent impedance matching theory, supplemented by the visualization of surface electric field distribution diagrams. Moreover, the dynamic tunability of the absorber is showcased by manipulating the Fermi level and relaxation time of the graphene metasurface. Additionally, the influence of geometric parameters within the graphene pattern on absorptivity is studied. The findings underscore the robustness of the graphene's geometry, particularly concerning its capacity to sustain resonance frequencies. Furthermore, the absorber's absorptivity is evaluated across a range of incident angles. The results suggest that the device effectively sustains significant absorption efficiency for both TE polarization in the range of 0° to 50° and TM polarization spanning from 0° to 40° . Finally, the absorber's potential for refractive index sensing within environmental contexts is demonstrated. The results suggest that the maximum sensitivity and FOM are $S_V = 1.75$ THz/RIU and $FOM_V = 12.774$ RIU $^{-1}$.

2. Structure and Design

The specific structure of the device is depicted in Figure 1, showcasing the detailed geometric parameters of our design. All parameters are outlined in Table 1. In this study, the graphene pattern comprises a Celtic cross and a ring divided into four sections. Gold (Au) serves as a reflector to impede the transmission of terahertz waves. Consequently, the thickness $t_m = 1$ μm is significantly greater than the skin depth. The device is deposited onto a silicon (Si) substrate.

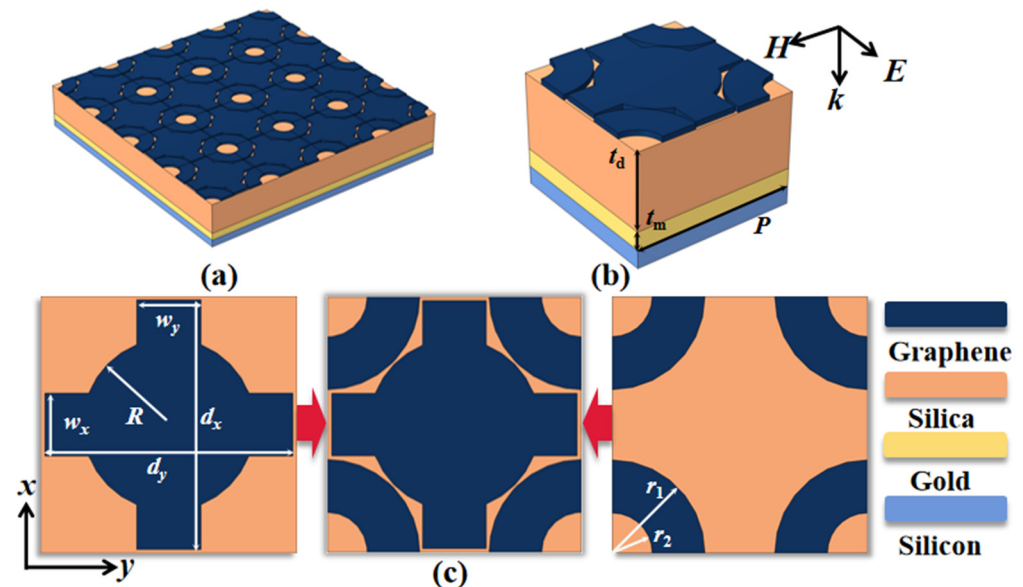


Figure 1. (a) A comprehensive view of the device; (b) a 3D representation of the unit structure; (c) a top-down perspective of the graphene unit pattern, comprising a Celtic cross and a ring divided into four sections.

Table 1. Geometric parameters of the device.

Name	P	t_d	t_m	w_x	w_y	d_x	d_y	R	A	r_1	r_2
Value (μm)	9	4.2	1	2.2	2.26	8.7	8.75	3.02	0.43	3.27	$r_1 \cdot A$

When an electromagnetic wave impacts the device, the graphene surface becomes excited, giving rise to the generation of surface plasmon waves (SPWs). If the frequency, wave vector, and propagation direction of the electromagnetic wave align with those of the SPW, the energy carried by photons is transferred to the free electrons of the SPW [33]. This phenomenon leads to surface plasmon resonance (SPR) [34]. Consequently, the device effectively captures the energy of the electromagnetic wave. The absorption characteristics of the device are characterized in the following manner [35]:

$$A = 1 - R - T \quad (1)$$

$$R = |S_{11}|^2 \quad (2)$$

$$T = |S_{21}|^2 \quad (3)$$

Here, R denotes reflectance, and T signifies transmittance. These quantities can also be represented using the S parameters, specifically the reflectance rate S_{11} and the transmittance rate S_{21} . In order to achieve $T = |S_{21}|^2 = 0$, the thickness of the Au layer must surpass its skin depth to inhibit the transmission of incident light. The skin depth of Au is defined as the distance at which the amplitude of the electromagnetic wave has attenuated to $1/e$ (approximately 37%) of its value at the surface [36]:

$$e^{-\alpha\delta} = 1/e \Rightarrow \delta = \frac{1}{\alpha} = \sqrt{\frac{2}{\omega\mu\sigma}} = \frac{1}{\sqrt{\pi f\mu\sigma}} \quad (4)$$

In this study, for gold (Au), the values used are $\mu = \mu_0 = 4\pi \times 10^{-7} \text{ N/A}^2$ and $\sigma = 4.56 \times 10^7 \text{ S/m}$. Consequently, the maximum skin depth within the frequency range of f (1~10 THz) is calculated to be $7.4531 \times 10^{-2} \mu\text{m}$, which is much smaller than t_m (1 μm).

In this context, transmission line theory and equivalent impedance matching theory are employed to analyze the objective of achieving $R = |S_{11}|^2 = 0$. According to the equivalent impedance matching theory, the equivalent impedance of the device is described as follows [37]:

$$Z_{\text{eff}} = \sqrt{\frac{(1 + S_{11})^2 - S_{21}^2}{(1 - S_{11})^2 - S_{21}^2}} = \frac{1 + S_{11}}{1 - S_{11}} (S_{21} = 0) \quad (5)$$

Therefore, perfect absorption is achieved when $S_{11} = 0$, $Z_{\text{eff}} = 1$, that is, when $\text{Re}(Z_{\text{eff}}) = 1$ and $\text{Im}(Z_{\text{eff}}) = 0$. In fact, S_{11} and R can be expressed according to Equation (5) as follows:

$$S_{11} = \frac{Z_{\text{eff}} - 1}{Z_{\text{eff}} + 1} = \frac{Z_{\text{eff}} \cdot Z_0 - Z_0}{Z_{\text{eff}} \cdot Z_0 + Z_0} = \frac{Z_{\text{in}} - Z_0}{Z_{\text{in}} + Z_0} \quad (6)$$

$$R = \left(\frac{Z_{\text{in}} - Z_0}{Z_{\text{in}} + Z_0} \right)^2 \quad (7)$$

Here, $Z_{\text{in}} = Z_{\text{eff}} \cdot Z_0$ signifies the input impedance of the graphene layer, where Z_0 represents the intrinsic impedance of free space. When Z_{in} equals Z_0 , indicating that the input impedance of the absorber matches the intrinsic impedance of free space, perfect absorption can be attained [38]. Equation (7) can be elucidated utilizing transmission line theory.

An equivalent circuit model can be established for the device [39], as shown in Figure 2. The absorber is equivalent to an RLC series circuit. Since the gold layer only functions to reflect the electromagnetic wave during absorption, it can be treated as a short circuit [40]. The impedance of the silicon dioxide layer and its input impedance are expressed as follows [41]:

$$\begin{cases} Z_1 = jZ_d \tan(k_d t_d) \\ Z_d = \sqrt{\mu_0 / \epsilon_0 \epsilon_d} \\ k_d = 2\pi f \sqrt{\epsilon_0 \epsilon_d \mu_0} \end{cases} \quad (8)$$

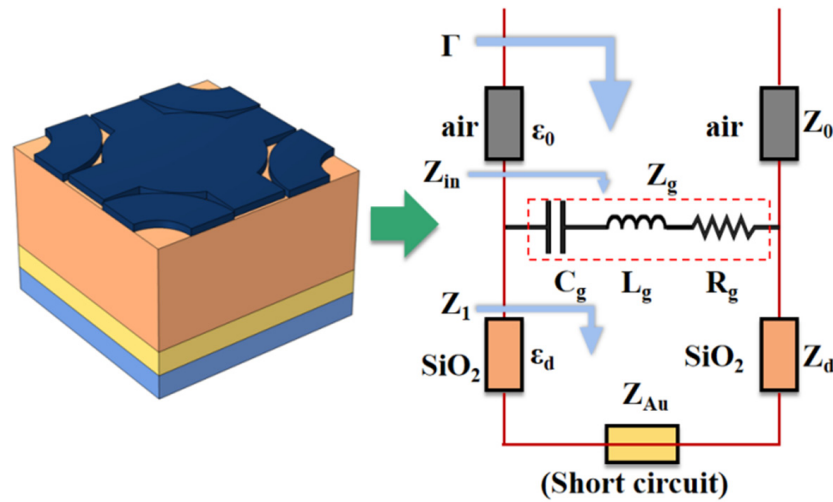


Figure 2. The equivalent circuit model of the absorber.

The impedance of the graphene layer is given by

$$Z_g = R_g + jX_g = R_g + j\left(2\pi f L_g - \frac{1}{2\pi f C_g}\right) \quad (9)$$

When SPR occurs at a certain incident electromagnetic wave frequency, the entire circuit is in a resonant state, exhibiting resistive behavior. Therefore,

$$X_g = 0 \Rightarrow Z_g = R_g \quad (10)$$

At this point, the input impedance of it is as follows:

$$Z_{in} = \frac{Z_1 \cdot Z_g}{Z_1 + Z_g} \quad (11)$$

The input impedance of the circuit is

$$\begin{cases} \Gamma = \frac{Z_{in} - Z_0}{Z_{in} + Z_0} = S_{11} \\ Z_0 = \sqrt{\frac{\mu_0}{\epsilon_0}} (Z_0 = 120\pi \approx 377\Omega) \end{cases} \quad (12)$$

Hence, $A = 1 - R$ can be described as follows: only when $Z_{in} = Z_0$, A reaches its maximum value.

$$A = 1 - R = 1 - |S_{11}|^2 = 1 - \Gamma^2 = 1 - \left(\frac{Z_{in} - Z_0}{Z_{in} + Z_0}\right)^2 = \frac{4}{\frac{Z_{in}}{Z_0} + \frac{Z_0}{Z_{in}} + 2} \quad (13)$$

In conclusion, achieving perfect absorption through the alignment of the absorber’s input impedance with the intrinsic impedance of free space necessitates a meticulous choice of several key factors. These factors include the incident frequency (f), the dielectric layer’s

material (ϵ_d) and thickness (t_d), as well as the impedance of graphene (Z_g). In terms of the dielectric layer, silica was selected due to its exceptional hardness and resistance to abrasion, which render it particularly well suited to the demanding operational conditions. The determination of the appropriate thickness for this layer will be explored in the subsequent section. The impedance of graphene is intricately tied to its relative permittivity, which is expressed as follows [42]:

$$\epsilon_g = 1 + j \frac{\sigma_g(\omega)}{\epsilon_0 \omega t_g} \quad (14)$$

where t_g represents the thickness of the graphene layer. In this study, a value of $t_g = 1$ nm was selected for ease of calculation purposes.

The total surface conductivity of graphene is defined as follows [43]:

$$\sigma_g(\omega) = \sigma_{\text{inter}}(\omega) + \sigma_{\text{intra}}(\omega) \quad (15)$$

where $\sigma_{\text{inter}}(\omega)$ denotes the interband conductivity of graphene, and $\sigma_{\text{intra}}(\omega)$ represents the intraband conductivity. These can be expressed using the classical Kubo formula [44]:

$$\sigma_{\text{inter}}(\omega) = \frac{ie^2}{4\pi\hbar^2} \ln \left[\frac{2|E_F| - \hbar(\omega + i\tau^{-1})}{2|E_F| + \hbar(\omega + i\tau^{-1})} \right] \quad (16)$$

$$\sigma_{\text{intra}}(\omega) = \frac{ie^2 k_B T}{\pi \hbar^2 (\omega + i\tau^{-1})} \left\{ \frac{E_F}{k_B T} + 2 \ln \left[\exp\left(-\frac{E_F}{k_B T}\right) + 1 \right] \right\} \quad (17)$$

where

e represents the elementary charge,

\hbar is the reduced Planck constant,

E_F signifies the Fermi energy level of graphene,

ω stands for the angular frequency of the incident electromagnetic wave,

τ is the relaxation time of graphene,

k_B denotes the Boltzmann constant,

T represents the ambient temperature in Kelvin.

According to the Pauli exclusion principle, within the terahertz range, where E_F is much greater than $\hbar\omega$, graphene's surface conductivity is primarily determined by intraband effects. As a result, the contribution of the interband conductivity $\sigma_{\text{inter}}(\omega)$ can be disregarded, leading to the simplification of $\sigma_g(\omega)$ using the Drude model [45] as follows:

$$\sigma_g(\omega) = \sigma_{\text{intra}}(\omega) = \frac{ie^2 |E_F|}{\pi \hbar^2 (\omega + i\tau^{-1})} \quad (18)$$

Based on the discussions presented above, it is evident that $\sigma_g(\omega)$ can be modulated by manipulating the frequency of incident light (ω or $f = 2\pi\omega$), the Fermi level (E_F), and the relaxation time (τ) of graphene. These dynamics are visually depicted in Figure 3, showcasing how graphene's surface conductivity changes with respect to the incident frequency and E_F at $\tau = 2.0$ ps, as well as concerning the incident frequency and τ at $E_F = 0.8$ eV. This provides a theoretical foundation for subsequent simulation results.

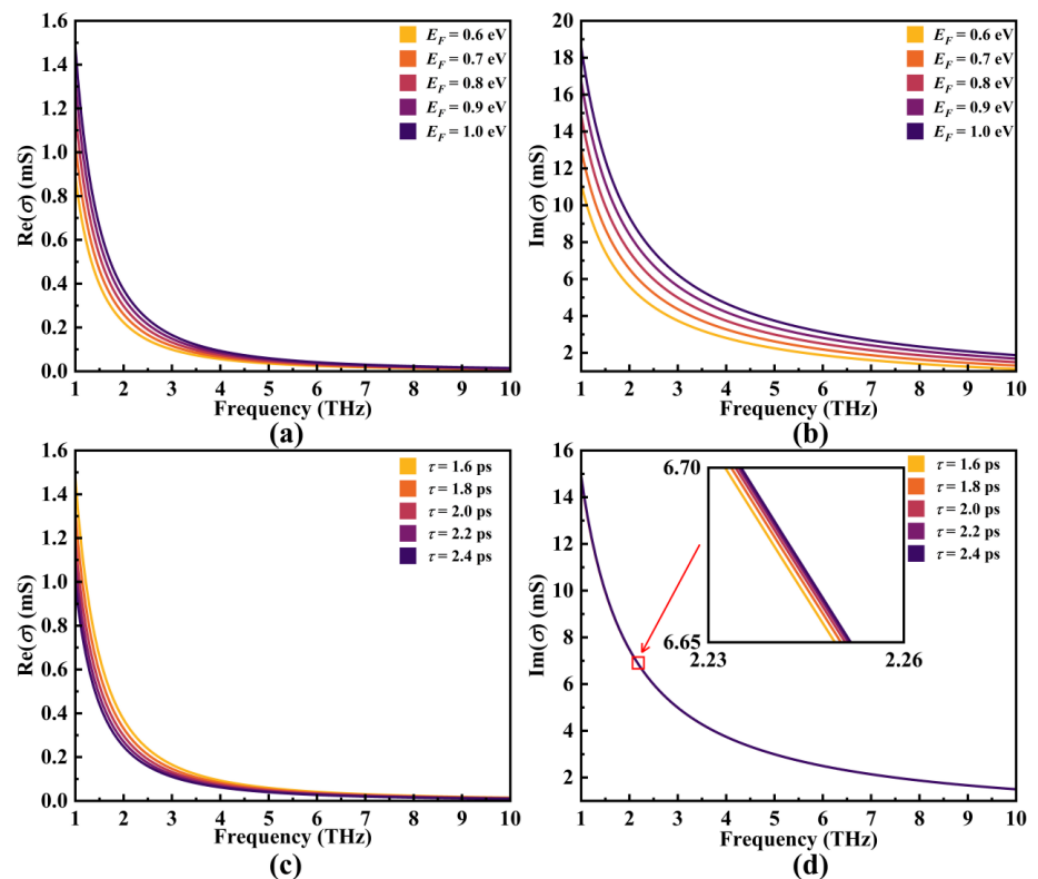


Figure 3. (a,b) The correlation between $\text{Re}(\sigma)$ and $\text{Im}(\sigma)$ with respect to the Fermi level (E_F) of graphene when $\tau = 2.0$ ps; (c,d) the connection between $\text{Re}(\sigma)$ and $\text{Im}(\sigma)$ in relation to the relaxation time (τ) when $E_F = 0.8$ eV.

3. Simulation Process

This section will explain the building of the proposed simulation model of a graphene terahertz absorber in COMSOL Multiphysics 5.6 software.

Following the construction of the model using the parameters listed in Table 1, an analyte, such as air, was added above the model. The thickness of the analyte is recommended to be greater than 30 μm . Next, the corresponding material parameters for each geometric part were added. The silicon substrate was not created during the simulation.

In the x - y plane, periodic boundary conditions were implemented, while perfect match layers were established in the z -direction to absorb the excess scattered waves. The transition boundary condition was applied to the graphene layer. The incident electromagnetic wave frequency was set between 1 and 10 THz. The excitation port was set above the analyte to simulate the incident electromagnetic wave, and the port was set below the gold layer to extract the S parameters. The “Type of port” was selected as “Periodic”.

For meshing, the sequence type was configured as “User-controlled mesh”. A new “Free triangular” mesh was created for the graphene layer, with the specified “Size” parameters. The “Maximum element size” was set to 0.2 μm , and the “Minimum element size” was set to 0.1 μm . The remaining meshing settings were left as default.

4. Simulation Results and Discussion

Distinct tests were conducted to evaluate the absorption performance of the absorber under both TE and TM polarizations, as depicted in Figure 4a. Five absorption peaks, designated as Modes I–V, are clearly discernible. Notably, apart from Mode V wherein a slight variance in absorption rate and resonance frequency is observed, the other modes remain essentially unaffected. This underscores the polarization independence of the

absorber’s absorption characteristics. Unless otherwise stipulated, all discussions in this study are grounded in TE polarization.

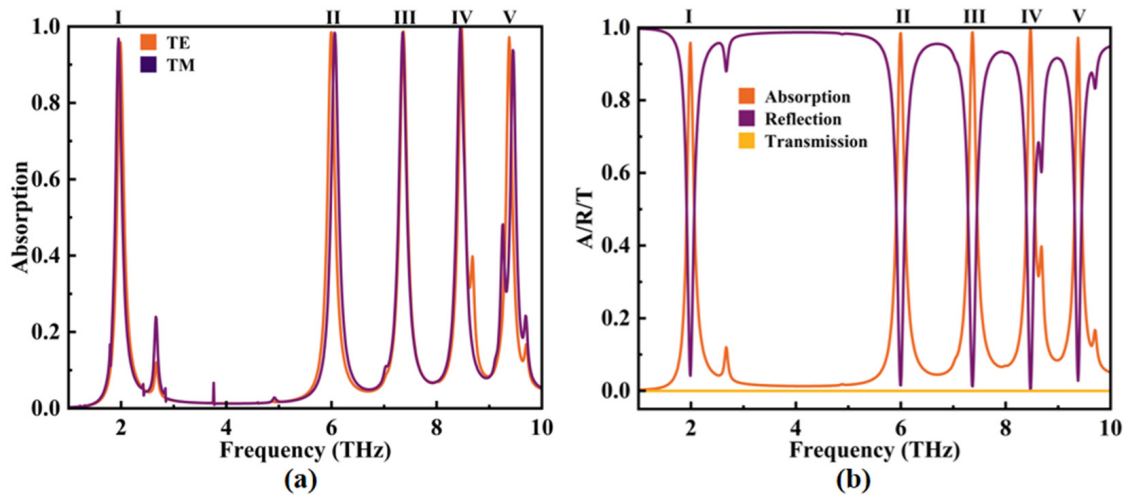


Figure 4. (a) The absorption rate diagrams of the device under TE polarization and TM polarization. (b) The A/R/T graph of the absorber under TE polarization.

The corresponding equivalent impedance matching diagrams for each mode were mapped as shown in Figure 5. It can be observed that, at these resonance frequencies, $Re(Z)$ is close to 1 and $Im(Z)$ is close to 0, especially for Mode IV (Figure 5d) with an absorption rate of 99.87%, $Re(Z) = 0.9958$, and $Im(Z) = -0.0769$, indicating a remarkably close approximation to perfect absorption. These experimental results align very closely with the theoretical derivations discussed earlier.

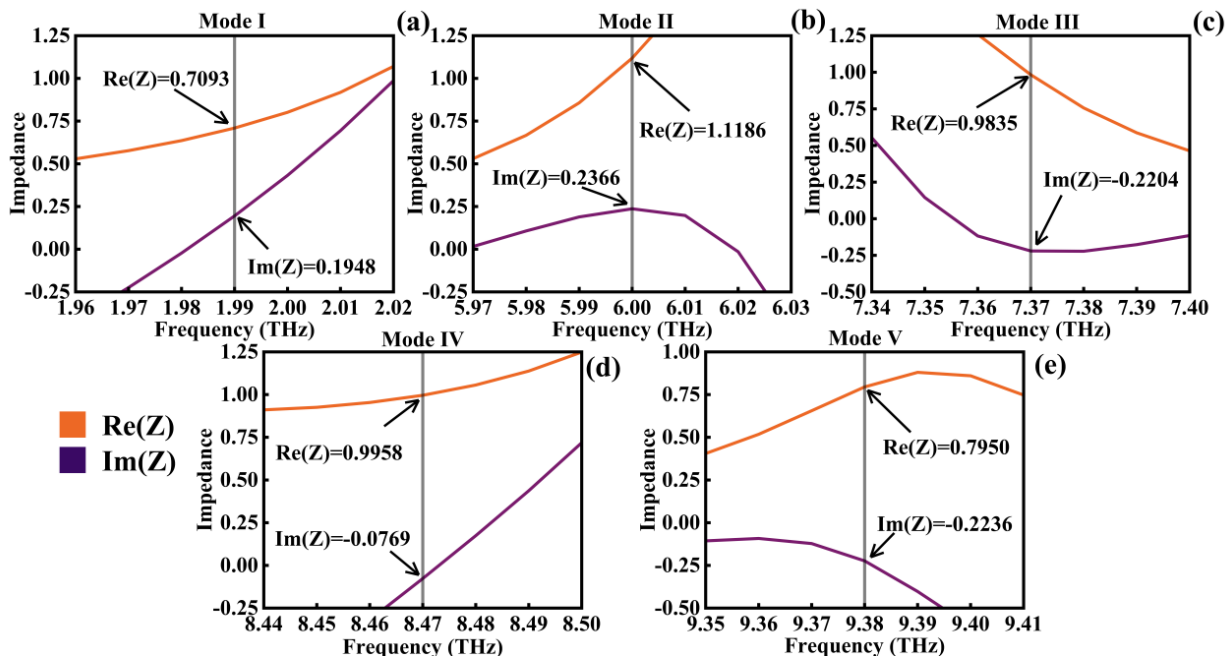


Figure 5. Equivalent impedance matching diagrams for Modes I–V (a–e).

As illustrated in Figure 6, the total absorption rate diagram of the device arises from the coupling of two subpatterns. It is evident that significant SPR occurs at five different resonant frequencies: $f_I = 1.99$ THz, $f_{II} = 6.00$ THz, $f_{III} = 7.37$ THz, $f_{IV} = 8.47$ THz, and $f_V = 9.38$ THz. The corresponding absorption rates for these modes were 95.82%, 98.47%, 98.72%, 99.87%, and 97.20%, respectively.

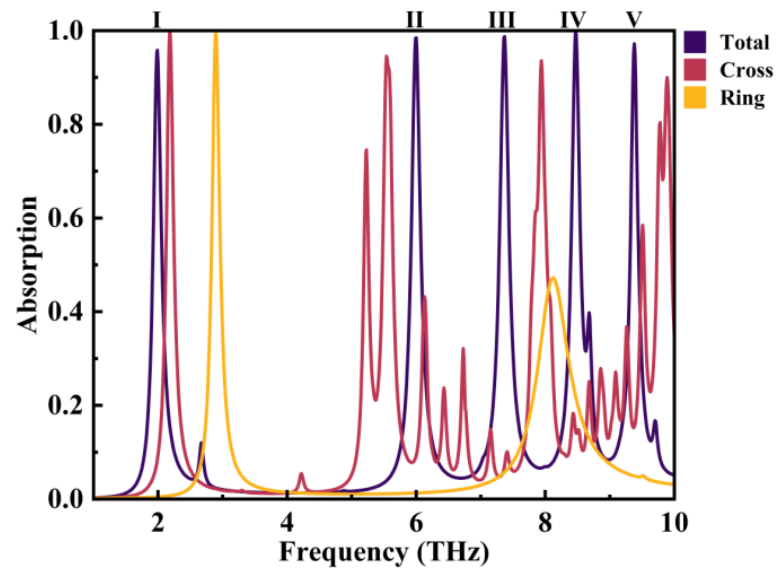


Figure 6. The absorption rate diagram of the device includes the overall absorption rate diagram of the entire geometric structure, along with absorption rate diagrams for two subpatterns.

To ascertain the precise positions at which LSPR occurs on the graphene patterns for each mode, electric field monitors were strategically positioned on the x–y plane. The resultant findings are visually depicted in Figure 7.

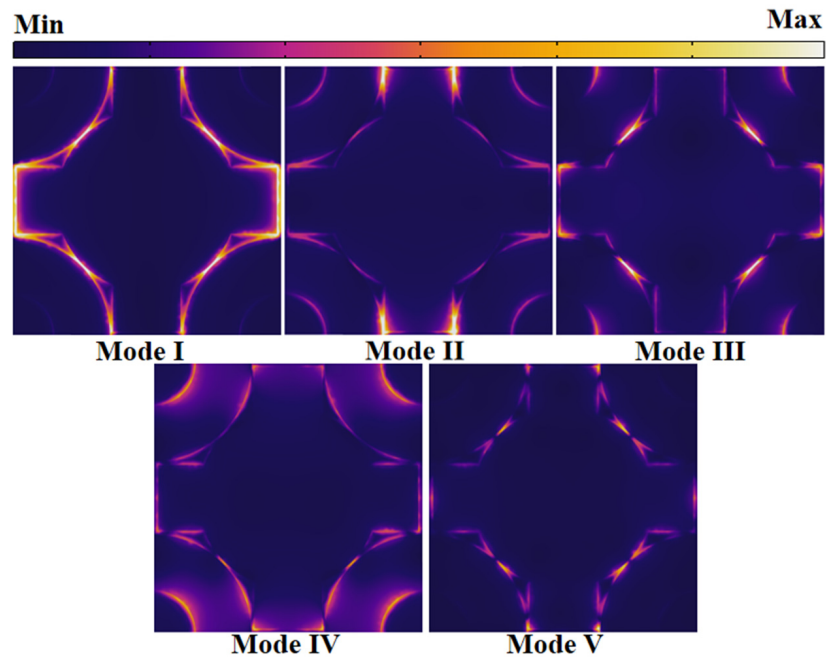


Figure 7. Surface electric field distribution maps of the five modes in the x–y plane.

In Mode I, localized surface plasmon resonance (LSPR) was predominantly concentrated in the proximity of the ring and the Celtic cross, extending along the cross’s edges in the y-direction. This behavior can be attributed to the coupling with neighboring periodic graphene patterns. Furthermore, regions along the ring’s edges exhibited a relatively weaker LSPR intensity. In Mode II, robust resonance was localized near the Celtic cross’s edges in the x-direction and the adjacent region of the ring. In contrast, other positions displayed subdued responses. Moreover, a relatively weaker surface plasmon resonance was discernible along the inner edge of the ring.

In Mode III, significant LSPR contributions were evident near the circular segment of the Celtic cross, particularly in proximity to the ring. Additionally, pronounced LSPR effects were observed along the Celtic cross's edges in the y-direction. For Mode IV, LSPR was conspicuous across several positions of the pattern, primarily along both sides of the ring's edges and the edges of the Celtic cross, coupled with adjacent periodic patterns.

In Mode V, LSPR predominantly emerged within the gaps between the Celtic cross and the ring. These gaps encompass the spaces between the circle and the ring, between the Celtic cross and the ring, and between the Celtic cross and the adjacent periodic cross.

Owing to the inherent symmetry of the graphene pattern, the regions in which LSPR is excited maintain symmetry as well [46]. This characteristic enhances the absorber's capability to sustain absorption performance across a broader range of incident angles. Throughout this paper, unless explicitly stated, all discussions are predicated on the scenario of normal electromagnetic wave incidence, where the incident angle (θ) is set at 0 degrees. Notably, in this study, it became apparent that the gaps between the subpatterns and their edges played a pivotal role in the occurrence of surface plasmon resonance [47,48]. Therefore, it is imperative to manipulate the geometric parameters of these regions to explore how variations impact the absorber's absorption performance.

Numerical analyses were performed on the geometric parameters of the graphene pattern (excluding r_2 , as it scales with r_1). Hence, this study focused solely on variations in the overall size of the ring. And the results are depicted in Figure 8. Overall, the alteration of various geometric parameters did not significantly shift the resonant frequencies of the five modes. This indicates that the geometric parameters of the graphene pattern exhibit robustness in affecting resonance frequencies. However, changing the geometric parameters can lead to relatively significant variations in the absorption rate. In summary, in this study, the gaps between subpatterns emerged as crucial in generating SPR and achieving high absorption rates. One of the techniques for designing multiband narrow-band metamaterial absorbers involves the thoughtful design of geometric patterns on the metasurface, creating multiple coupling regions. If the frequencies at which SPR occurs are continuous, maintaining elevated absorption rates across a range of frequencies, it becomes possible to devise a wideband SPR metamaterial absorber [49,50]. The geometric parameters of a graphene metasurface play a significant role in influencing the absorption of light based on the incident angle or polarization state. For instance, a graphene surface with high symmetry can maintain a consistently high absorption rate across a wide range of incident angles. Adjusting the geometric parameters allows for narrowing the absorption angle range or shifting the resonance frequency. Additionally, a graphene metasurface with a chiral pattern can selectively absorb light waves of a specific polarization state, and modifying the geometric parameters can alter its polarization selectivity. Modifying the geometric parameters directly influences the surface conductivity of graphene, consequently altering the impedance of the absorber. Inadequate geometric design can lead to suboptimal impedance matching, resulting in unsatisfactory absorption performance. On the other hand, well-designed geometric parameters not only enhance the robustness of the graphene pattern but also enable effective impedance matching within a specific resonance frequency range. Additionally, they ensure broad-angle absorption capabilities.

Furthermore, the impact of the thickness of the silica layer on absorption performances was tested, as depicted in Figure 9. At lower frequencies, reducing the thickness of the silica layer enhanced the absorption rate. Conversely, at higher frequencies, it is advisable to avoid an excessively thick silicon dioxide layer. This rule can be found in reference [51]. The graphene layer and the gold layer form an asymmetric Fabry–Perot cavity. Quoting the formula, the total reflection coefficient of the device can be expressed as follows:

$$\begin{aligned} r &= r_{12} + r_m = r_{12} + \frac{t_{12}t_{21}r_{23}e^{-2i\phi}}{1-r_{21}r_{23}e^{-2i\phi}} \\ \phi &= k_0nd \cos \theta' \end{aligned} \quad (19)$$

where d presents the thickness of the dielectric layer (t_d in this paper). When light is incident on the absorber, the graphene surface generates LSPR, and the light waves undergo multiple reflections within the Fabry–Perot cavity. By carefully selecting the appropriate material and thickness for the dielectric layer, the interference of the reflected light from different orders can be effectively suppressed. This leads to the occurrence of Fabry–Perot resonance, where the Fabry–Perot resonance and the LSPR on the graphene surface are strongly coupled. As a result, the electromagnetic waves are efficiently absorbed. After multiple experiments, it was determined that the average highest absorption rate for the five modes was achieved when $t_d = 4.2 \mu\text{m}$.

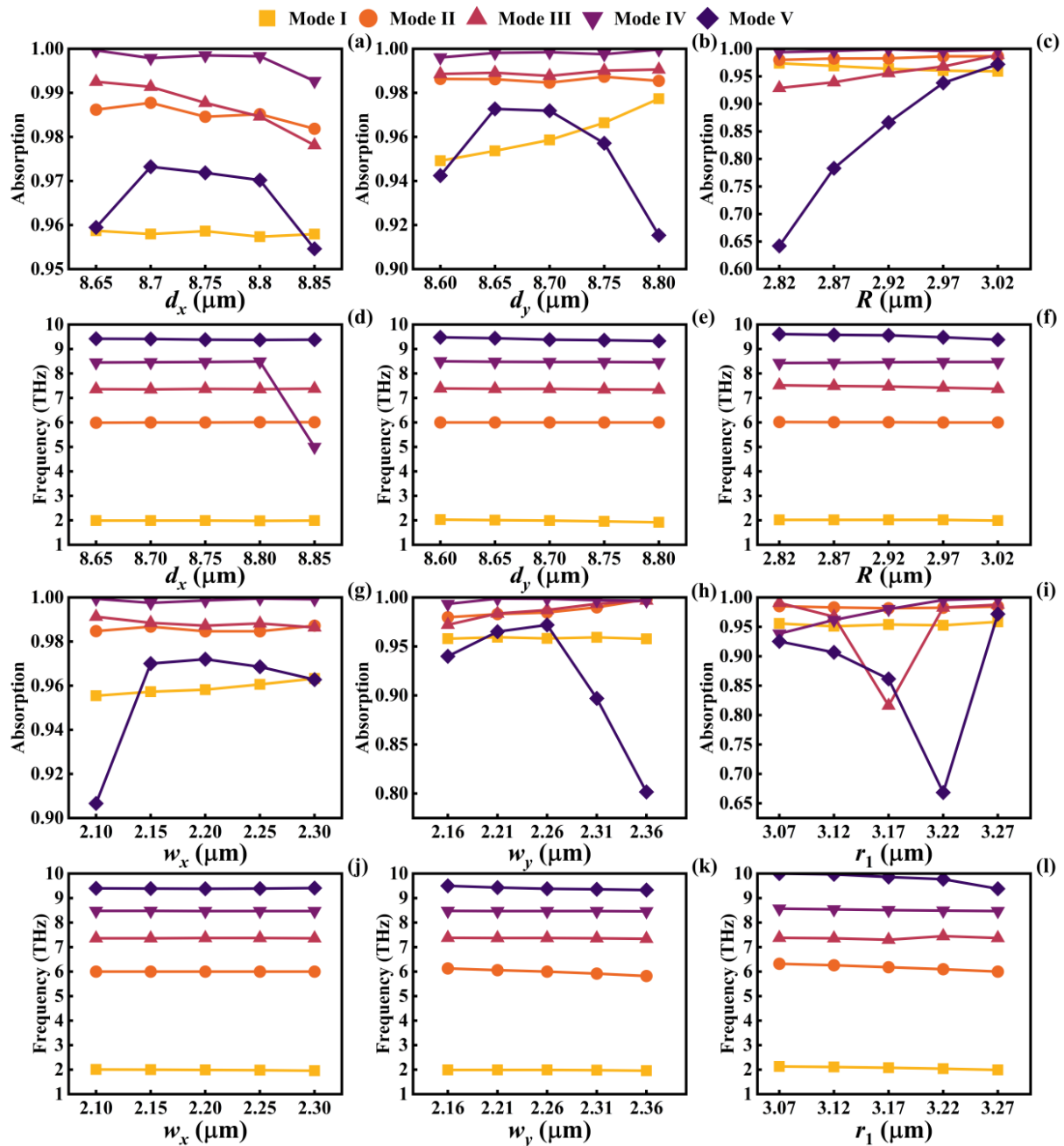


Figure 8. The impact of variations in geometric parameters on the absorber’s absorption rates (a–c,g–i) and resonance frequencies (d–f,j–l).

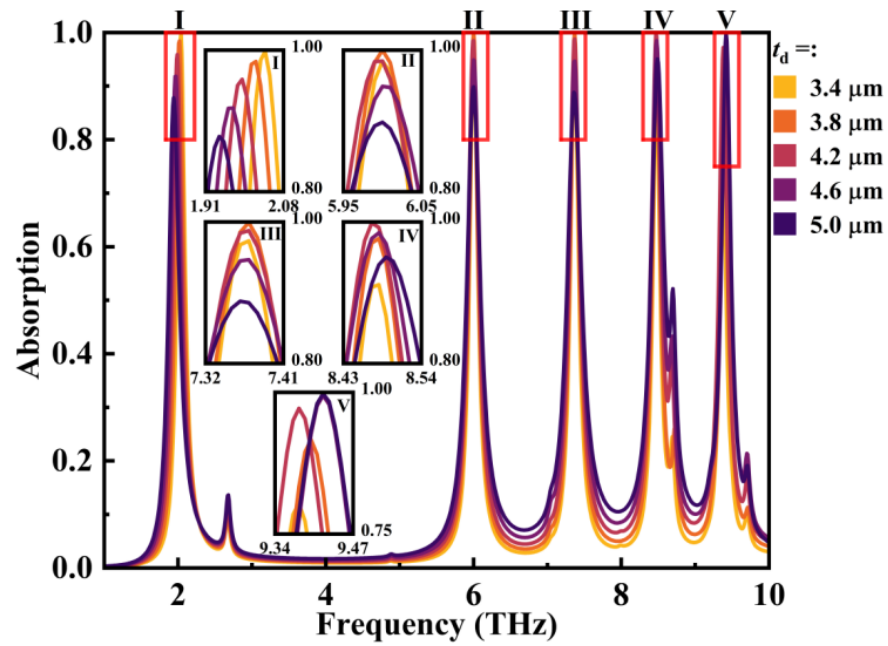


Figure 9. The impact of the thickness of the SiO₂ layer on absorptivity of the device.

Next, the dynamic tunability of the device was demonstrated by varying the Fermi level (E_F) and relaxation time (τ) of graphene. The effect of varying the Fermi level (E_F) under a relaxation time (τ) of 2.0 ps on the absorption performance of the absorber was initially examined. As shown in Figure 10, it is evident that with increasing E_F , the resonance frequencies of the five modes all experienced a blue shift. This shift occurs because the wavevector of surface plasmon polaritons (SPPs) satisfies the following relationship [52]:

$$k_{spp} \propto \hbar f_r^2 / (2\alpha_0 E_F c) \tag{20}$$

where α_0 is fine structure constant and f_r is resonance frequency. Hence, there exists a relationship between the Fermi level and resonance frequency:

$$f_r \propto E_F^{1/2} \tag{21}$$

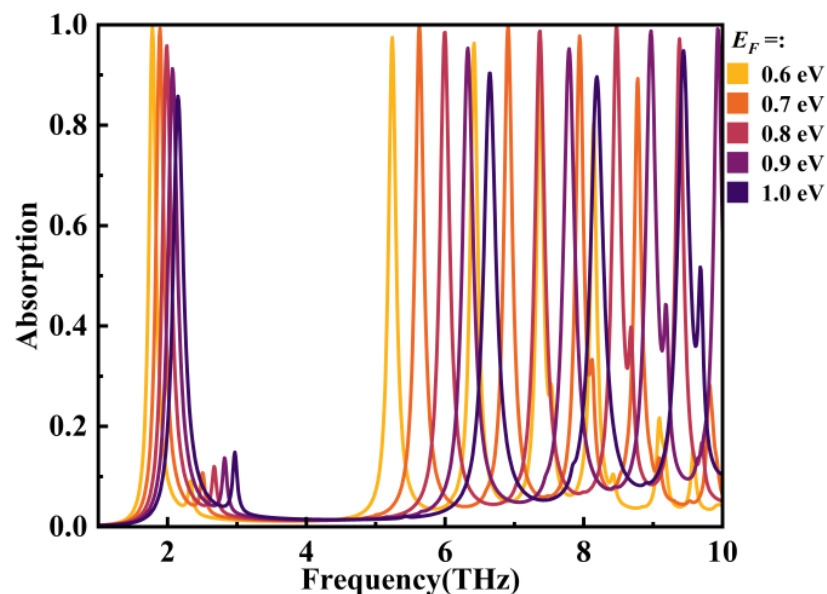


Figure 10. The impact of variations in E_F under $\tau = 2.0$ ps on the absorber’s absorption performance.

Therefore, the resonance frequency will increase with an increase in E_F , and the modulation bandwidth at higher frequencies will also be larger. There is a relationship between the Fermi level and the applied voltage [53],

$$E_F = V_F \sqrt{\frac{\pi \epsilon_0 \epsilon_r V_g}{e_0 t_d}} \quad (22)$$

where

V_F is the Fermi velocity, with a typical value of approximately 10^6 m/s,
 ϵ_0 and ϵ_r are the vacuum permittivity and relative permittivity, respectively,
 V_g is the applied external voltage,
 e_0 is the elementary charge,
 t_d is the thickness of the dielectric (SiO_2) layer.

It is apparent that, by maintaining a constant thickness of the dielectric layer, the magnitude of E_F can be controlled through the manipulation of the applied external voltage (V_g). In practical applications, once the device is fabricated, its absorption performance remains fixed. By applying a gate voltage, the capacity to dynamically adjust the Fermi level of graphene is gained, thereby influencing its conductivity. This dynamic capability allows the device to dynamically fine-tune both the absorption rate and resonance frequency, thereby ensuring optimal performance.

Subsequently, the changes in absorber performance were examined in relation to the relaxation time (τ) at a fixed Fermi level (E_F) of 0.8 eV. The outcomes of this investigation are depicted in Figure 11. As τ increased from 1.6 ps to 2.4 ps, the resonance frequencies of each mode remained constant, with only the absorption rate being modulated. This observation is consistent with the connection between the relaxation time of graphene and the Fermi level, as illustrated by the following relationship [54]:

$$\tau = E_F v / (e V_F^2) \quad (23)$$

where v represents the carrier mobility of graphene. With τ increasing from 1.6 ps to 2.4 ps, the resonant frequencies of each mode remained unaffected, while only the absorption rate underwent modulation. Since E_F remains constant, alterations in τ induce variations in the concentration of graphene carriers, subsequently influencing the intensity of plasmonic oscillations [55,56]. This cascade effect ultimately leads to changes in the absorption rate. In conclusion, the manipulation of graphene's Fermi level and relaxation time allows for effective control over the absorption rate and resonance frequency of graphene-based SPR metamaterial absorbers. In comparison to noble metal SPR metamaterial absorbers, our device exhibits the potential for broader practical applications.

According to the Fresnel equations, the transverse electric and transverse magnetic reflectances of the metamaterial absorber are, respectively, expressed as follows [57,58]:

$$\begin{cases} R_{\text{TE}} = \left| \frac{\cos \theta - \mu_r^{-1} \sqrt{n^2 - \sin^2 \theta}}{\cos \theta + \mu_r^{-1} \sqrt{n^2 - \sin^2 \theta}} \right|^2 \\ R_{\text{TM}} = \left| \frac{\epsilon_r \cos \theta - \sqrt{n^2 - \sin^2 \theta}}{\epsilon_r \cos \theta + \sqrt{n^2 - \sin^2 \theta}} \right|^2 \end{cases} \quad (24)$$

$$n = \sqrt{\epsilon_r \mu_r} \quad (25)$$

where θ represents the incident angle of the electromagnetic wave, and n denotes the effective refractive index of the metamaterial absorber. Taking TE polarization as an example, when the electromagnetic wave is normally incident, that is, $\theta = 0^\circ$, the expression for R_{TE} in Equation (23) can be written as follows:

$$R_{\text{TE}} = \left| \frac{\sqrt{\mu_r} - \sqrt{\epsilon_r}}{\sqrt{\mu_r} + \sqrt{\epsilon_r}} \right|^2 = \left| \frac{Z - Z_0}{Z + Z_0} \right|^2 \quad (26)$$

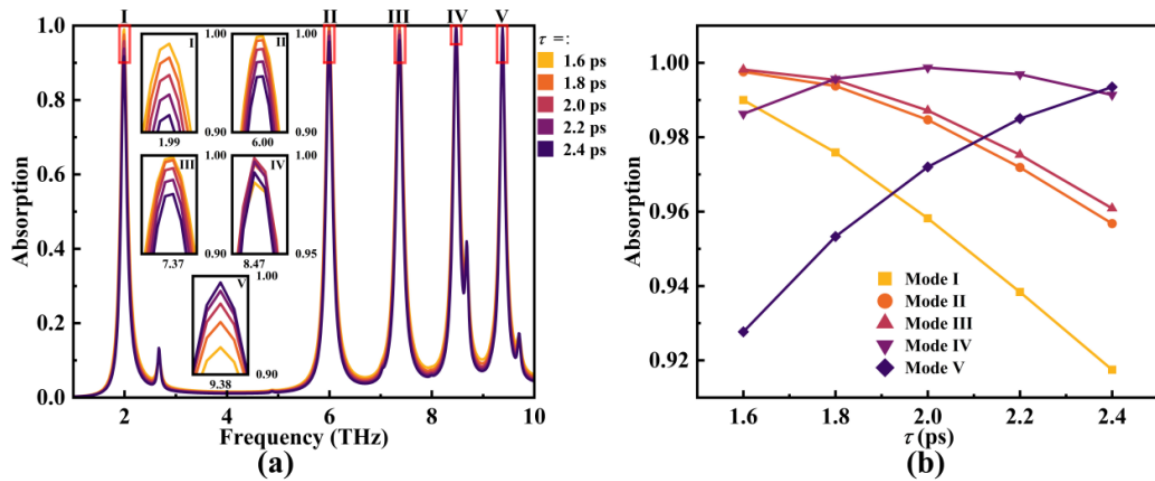


Figure 11. The influence of τ variation on the resonant frequency (a) and absorption performance (b) of the absorber under the condition of $E_F = 0.8$ eV.

This finding correlates with Equation (7). Moreover, Equation (23) emphasizes that the effect of graphene’s impedance is not solely limited to polarization modes; the incident angle of the electromagnetic wave also holds significant influence. Consequently, it is essential to conduct a thorough investigation into how the incident angle affects the absorption performance of the absorber. To address this, an incident angle ranging from 0° to 50° for TE polarization and from 0° to 40° for TM polarization was set up. The simulation outcomes are graphically presented in Figure 12.

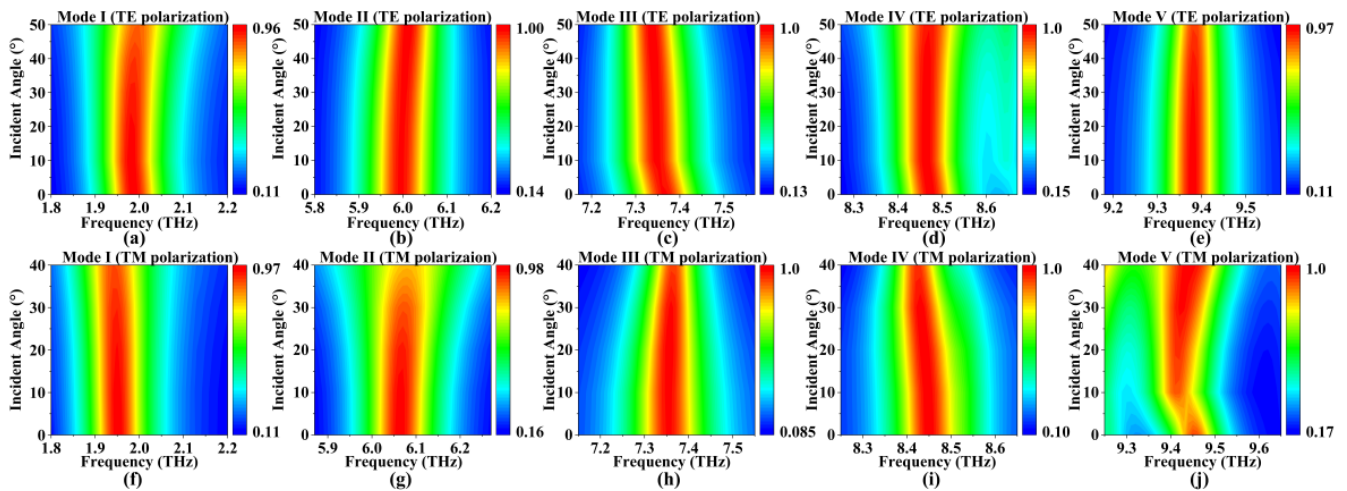


Figure 12. (a–e) The variation in the absorption performance with incident angle under TE polarization; (f–j) the changes in absorptivity with incident angle under TM polarization.

Under TE polarization, as the incident angle varied from 0 to 50 degrees, slight shifts in resonant frequencies were observed for each mode, while the absorption rates consistently remained above 85%. Similarly, in the case of TM polarization, in which the incident angle spanned from 0 to 40 degrees, each mode displayed minor resonant frequency shifts, while the absorption rates consistently stayed above 82%. This observation underscores the device’s capability to maintain substantial absorption rates even at larger incident angles. This phenomenon can be attributed to two key factors. Firstly, the device’s dimensions are smaller than the vacuum wavelength of the incident light, allowing it to effectively interact with a wide range of angles [59,60]. Additionally, the inherent symmetry of the graphene patterns plays a crucial role. Within a specific range of incident angles, the symmetry of the

graphene patterns remains intact, ensuring robust SPR at the corresponding positions as illustrated in Figure 7.

In summation, our design exhibited remarkable insensitivity to incident angles, encompassing a range from 0 to 50 degrees in the TE mode and 0 to 40 degrees in the TM mode. For practical applications, the incorporation of concave structures positioned above the absorber’s surface could be explored [61,62]. This strategic approach could facilitate the coupling of incident light with the graphene metasurface at specific angles, thus ensuring a consistently high absorption rate.

A pivotal performance aspect of the metamaterial SPR absorber is its capability for refractive index (RI) sensing. An analyte refractive index (n) range of 1.00 to 1.08 was selected, and the resulting shifts in the resonant frequencies and absorption rates were explored. The outcomes are visualized in Figure 13. Notably, as the refractive index increased, all five modes exhibited a pronounced red-shift in their resonant frequencies, with their absorption rates consistently maintained above 94.9%.

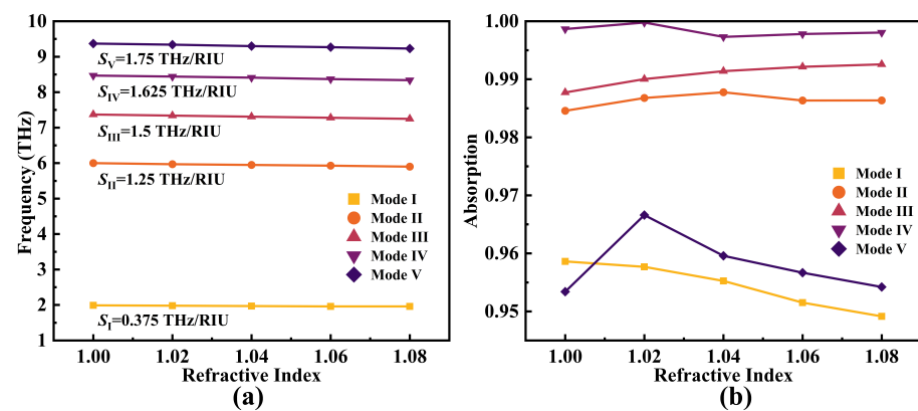


Figure 13. The variation in resonant frequencies (a) and absorption rates (b) of each mode as the ambient refractive index changes from 1.00 to 1.08.

The ranges of variation for these shifts were Δf_I : 1.96~1.99 THz, Δf_{II} : 5.9~6 THz, Δf_{III} : 7.25~7.37 THz, Δf_{IV} : 8.34~8.47 THz, and Δf_V : 9.23~9.37 THz, respectively. The sensitivity S is defined as follows [63]:

$$S = \frac{\Delta f}{\Delta n} \tag{27}$$

where Δn was 0.08 in this research. Hence, the corresponding S for each mode were $S_I = 0.375$ THz/RIU, $S_{II} = 1.25$ THz/RIU, $S_{III} = 1.5$ THz/RIU, $S_{IV} = 1.625$ THz/RIU, and $S_V = 1.75$ THz/RIU, respectively. The average sensitivity was $S_{avg} = 1.3$ THz/RIU, where RIU refers to the refractive index unit. According to the obtained results, the device was highly responsive to changes in the refractive index of the analyte, making it suitable for deployment as a refractive index sensor (RI sensor).

The figure of merit (FOM) is another crucial factor for assessing the sensing performance of the absorber. It is defined as follows [64,65]:

$$FOM = \frac{S}{FWHM} \tag{28}$$

where FWHM represents the full width at half maximum of the absorption peak. As indicated by Equation (27), Table 2 presents the average FWHM and FOM values for the device. Meanwhile, Table 3 and Figure 14 provides insight into the minimum FWHM for each mode along with its corresponding maximum FOM.

Table 2. FWHM_{avg} and FOM_{avg} for each mode as RI varies within the range of 1.00 to 1.08.

Mode	I	II	III	IV	V
FWHM _{avg} (GHz)	153.8	170	172.4	160.4	140.4
FOM _{avg} (RIU ⁻¹)	2.438	7.353	8.703	10.134	12.469

Table 3. FWHM_{min} and FOM_{max} for each mode as RI varies within the range of 1.00 to 1.08.

Mode	I	II	III	IV	V
FWHM _{min} (GHz)	151	170	169	157	137
FOM _{max} (RIU ⁻¹)	2.483	7.353	8.876	10.350	12.774

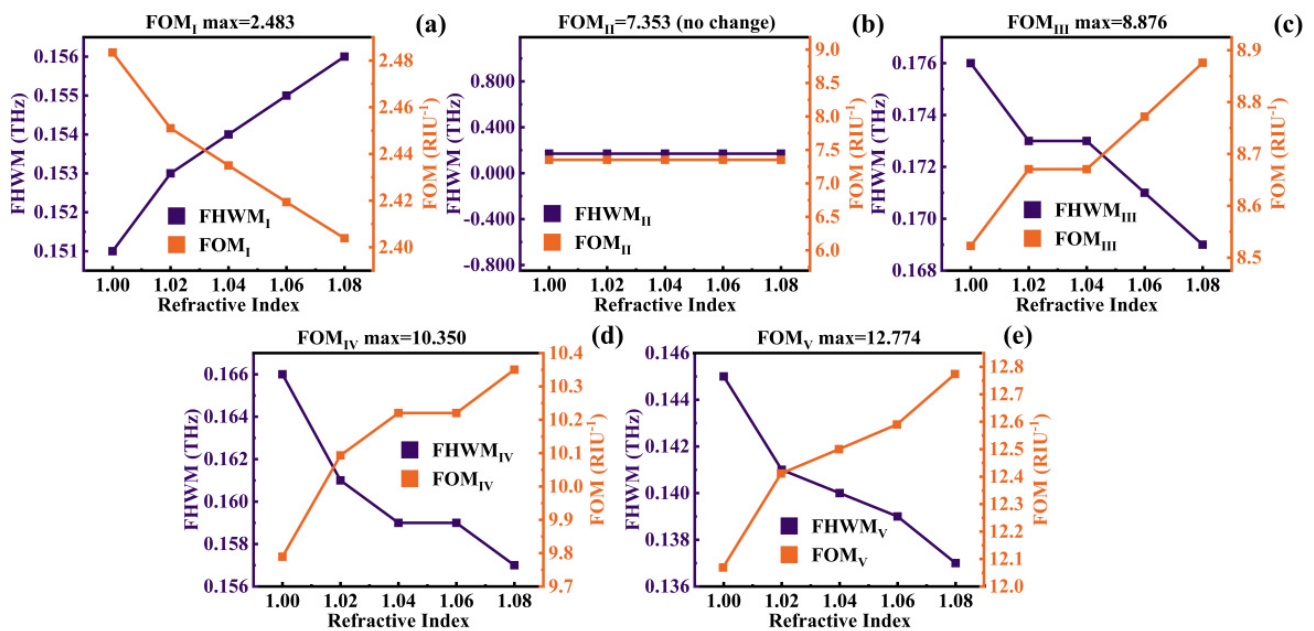


Figure 14. The variation in the FWHM and FOM of Mode I–V (a–e) with *n* ranges from 1.00 to 1.08.

From the results, it can be inferred that the absorber achieved a minimum FWHM of 137 GHz and a maximum FOM of 12.774 RIU⁻¹. This underscores the absorber’s strong sensing capabilities and resonance frequency selectivity. Lastly, in order to provide a comprehensive assessment of the absorber’s performance, a comparative analysis between the device and other metamaterial SPR absorbers was conducted. The results are presented in Table 4.

Table 4. Comparison with previous studies.

References	[43]	[66]	[32]	[67]	[68]	This Work
Number of absorption peaks	1	1	3	3	5	5
Tunability	Yes	No	Yes	Yes	Yes	Yes
S _{max} (THz/RIU)	1.57	2.1	2.00	1.867	0.066	1.75
FOM _{max} (RIU ⁻¹)	24.5	7.03	9.58	2.14	N/A	12.774

It is clear that our design, when compared with previous studies, exhibits a higher number of absorption peaks and a substantial improvement in refractive index sensing performance (FOM). This strongly indicates the device’s considerable potential for application in fields like biochemistry and sensing.

5. Conclusions

In summation, this study presents a new SPR terahertz absorber based on a single-layer, patterned graphene metasurface. Through rigorous theoretical exploration and meticulous numerical simulations, the penta-band absorption, dynamic tunability, geometric robustness, polarization independence, wide-angle absorption, and great sensing capacity of the absorber were elucidated. Compared with other works, the device features a simple structure that not only widens the number of absorption peaks but also ensures a high absorption rate and great refractive index sensing performance. Our work promotes diversity in the design of graphene-based metamaterial absorbers, offering fresh design inspiration. Consequently, we believe this novel SPR metamaterial absorber holds promising potential for applications in active optoelectronic devices, modulators, optical stealth, RI sensors, and other related fields.

Author Contributions: R.L.: conceptualization, formal analysis, investigation, data curation, writing—original draft, writing—review and editing. H.C.: conceptualization, formal analysis, investigation, data curation, writing—review and editing. Z.Z.: conceptualization, formal analysis, investigation, data curation, funding acquisition. Z.Y.: conceptualization, formal analysis, investigation, data curation, writing—original draft, writing—review and editing. B.T.: conceptualization, formal analysis, investigation. J.C.: conceptualization, formal analysis, investigation, data curation. Y.Y.: conceptualization, formal analysis, investigation, data curation. C.T.: conceptualization, formal analysis, investigation, data curation, funding acquisition. J.Z.: conceptualization, data curation, funding acquisition. T.S.: conceptualization, formal analysis, investigation, data curation. All authors have read and agreed to the published version of the manuscript.

Funding: The authors are grateful to the support by National Natural Science Foundation of China (No. 51606158, 11604311, 61705204, 21506257); the Funded by the Basic Research Program of Shanxi Province (202103021223353); the funded by the Open Fund of the Key Laboratory for Metallurgical Equipment and Control Technology of Ministry of Education in Wuhan University of Science and Technology, China (No. MECOF2022B01); the Funded by the Open Fund of Hubei Key Laboratory of Mechanical Transmission and Manufacturing Engineering at Wuhan University of Science and Technology (MTMEOF2021B02).

Institutional Review Board Statement: Not applicable.

Informed Consent Statement: Not applicable.

Data Availability Statement: Publicly available datasets were analyzed in this study. This data can be found here: <https://www.lumerical.com/> (accessed on 1 January 2020).

Conflicts of Interest: The authors declare no conflict of interest.

References

1. Krasikov, S.; Tranter, A.; Bogdanov, A.; Kivshar, Y. Intelligent metaphotonics empowered by machine learning. *Opto Electron. Adv.* **2022**, *5*, 210147. [CrossRef]
2. Wu, F.Y.; Shi, P.C.; Yi, Z.; Li, H.L.; Yi, Y.G. Ultra-Broadband Solar Absorber and High-Efficiency Thermal Emitter from UV to Mid-Infrared Spectrum. *Micromachines* **2023**, *14*, 985. [CrossRef]
3. Biabanifard, M.; Abrishamian, M.S. Circuit Modeling of Tunable Terahertz Graphene Absorber. *Optik* **2018**, *158*, 842–849. [CrossRef]
4. Yang, J.; Lin, Y.-S. Design of Tunable Terahertz Metamaterial Sensor with Single- and Dual-Resonance Characteristic. *Nanomaterials* **2021**, *11*, 2212. [CrossRef]
5. Song, Z.; Wang, K.; Li, J.; Liu, Q.H. Broadband Tunable Terahertz Absorber Based on Vanadium Dioxide Metamaterials. *Opt. Express* **2018**, *26*, 7148–7154. [CrossRef]
6. Shen, Y.; Liang, L.; Zhang, S.; Huang, D.; Zhang, J.; Xu, S.; Liang, C.; Xu, W. Thermally and Electrically Dual-Tunable Absorber Based on Dirac Semimetal and Strontium Titanate. *Nanoscale* **2018**, *10*, 1622–1630. [CrossRef]
7. Wu, X.; Yin, C.; Zhang, M.; Xie, Y.; Hu, J.; Long, R.; Wu, X.; Wu, X. The Intercalation Cathode of MOFs-driven Vanadium-based Composite Embedded in N-doped Carbon for Aqueous Zinc ion Batteries. *Chem. Eng. J.* **2023**, *452*, 139573. [CrossRef]
8. Li, J.; Liu, G.; Liu, B.; Min, Z.; Qian, D.; Jiang, J.; Li, J. An extremely facile route to Co₂P encased in N,P-codoped carbon layers: Highly efficient bifunctional electrocatalysts for ORR and OER. *Int. J. Hydrogen Energy* **2018**, *43*, 1365–1374. [CrossRef]
9. Chen, Z.H.; Cai, P.G.; Wen, Q.Y.; Chen, H.; Tang, Y.J.; Yi, Z.; Wei, K.H.; Li, G.F.; Tang, B.; Yi, Y.G. Graphene Multi-Frequency Broadband and Ultra-Broadband Terahertz Absorber Based on Surface Plasmon Resonance. *Electronics* **2023**, *12*, 2655. [CrossRef]

10. Li, K.; Yu, J. Photonics-Aided Terahertz-Wave Wireless Communication. *J. Light. Technol.* **2022**, *40*, 4186–4195. [[CrossRef](#)]
11. Liang, S.R.; Xu, F.; Li, W.X.; Yang, W.X.; Cheng, S.B.; Yang, H.; Chen, J.; Yi, Z.; Jiang, P.P. Tunable smart mid infrared thermal control emitter based on phase change material VO₂ thin film. *Appl. Therm. Eng.* **2023**, *232*, 121074. [[CrossRef](#)]
12. Kats, M.A.; Capasso, F. Optical Absorbers Based on Strong Interference in Ultra-thin Films. *Laser Photonics Rev.* **2016**, *10*, 735–749. [[CrossRef](#)]
13. Kazanskiy, N.L.; Khonina, S.N.; Butt, M.A. Recent Development in Metasurfaces: A Focus on Sensing Applications. *Nanomaterials* **2023**, *13*, 118. [[CrossRef](#)]
14. Abou Houran, M.; Alsharai, M.; Baqir, M.A.; Saqlain, M.; Dhasarathan, V. Polarization-Insensitive and Wide-Angle Absorber Operating in the Visible and near-Infrared Regimes. *Optik* **2023**, *283*, 170915. [[CrossRef](#)]
15. Zou, Y.; Chen, S.; Sun, J.; Zhou, S. Mid-Infrared Pyroelectric Detector with Metasurface Electrode for Broadband Enhanced Absorption. *J. Phys. D Appl. Phys.* **2023**, *56*, 445105. [[CrossRef](#)]
16. Bouanane, I.; Bedu, F.; Ozerov, I.; Sciacca, B.; Santinacci, L.; Duché, D.; Berginc, G.; Escoubas, L.; Margeat, O.; Le Rouzo, J. Design of Infrared Optical Absorber Using Silver Nanorings Array Made by a Top-down Process. *Sci. Rep.* **2023**, *13*, 7770. [[CrossRef](#)] [[PubMed](#)]
17. Li, S.-J.; Wu, P.-X.; Xu, H.-X.; Zhou, Y.-L.; Cao, X.-Y.; Han, J.-F.; Zhang, C.; Yang, H.-H.; Zhang, Z. Ultra-Wideband and Polarization-Insensitive Perfect Absorber Using Multilayer Metamaterials, Lumped Resistors, and Strong Coupling Effects. *Nanoscale Res. Lett.* **2018**, *13*, 386. [[CrossRef](#)] [[PubMed](#)]
18. Vafapour, Z.; Ghahraloud, H.; Keshavarz, A.; Islam, M.S.; Rashidi, A.; Dutta, M.; Stroschio, M.A. The Potential of Refractive Index Nanobiosensing Using a Multi-Band Optically Tuned Perfect Light Metamaterial Absorber. *IEEE Sens. J.* **2021**, *21*, 13786–13793. [[CrossRef](#)]
19. Liang, Y.; Lin, H.; Lin, S.; Wu, J.; Li, W.; Meng, F.; Yang, Y.; Huang, X.; Jia, B.; Kivshar, Y. Hybrid Anisotropic Plasmonic Metasurfaces with Multiple Resonances of Focused Light Beams. *Nano Lett.* **2021**, *21*, 8917–8923. [[CrossRef](#)]
20. Stewart, J.W.; Nebabu, T.; Mikkelsen, M.H. Control of Nanoscale Heat Generation with Lithography-Free Metasurface Absorbers. *Nano Lett.* **2022**, *22*, 5151–5157. [[CrossRef](#)]
21. Qi, Y.; Yang, L.; Yue, L.; Li, J.; Wang, X.; Sun, Z.; Cao, J. Theoretical Studies of the THz Compression of Low-to-Medium Energy Electron Pulses and the Single-Shot Stamping of Electron–THz Timing Jitter. *N. J. Phys.* **2021**, *23*, 063052. [[CrossRef](#)]
22. Sun, S.; Liu, S.; Zhong, S. Analysis of Terahertz Wave Penetration Capacity to 2D Conductive Cylinder Coated with Steady-State Parabolic Distribution Plasma Media. *Results Phys.* **2021**, *27*, 104516. [[CrossRef](#)]
23. Shi, S.-C.; Paine, S.; Yao, Q.-J.; Lin, Z.-H.; Li, X.-X.; Duan, W.-Y.; Matsuo, H.; Zhang, Q.; Yang, J.; Ashley, M.C.B.; et al. Terahertz and Far-Infrared Windows Opened at Dome A in Antarctica. *Nat. Astron.* **2016**, *1*, 0001. [[CrossRef](#)]
24. Bowman, T.C.; El-Shenawee, M.; Campbell, L.K. Terahertz Imaging of Excised Breast Tumor Tissue on Paraffin Sections. *IEEE Trans. Antennas Propag.* **2015**, *63*, 2088–2097. [[CrossRef](#)]
25. Mason, M.J.; Coleman, B.J.; Saha, S.; Mustafa, M.M.; Green, M.J. Graphene Signatures: Identifying Graphite and Graphene Grades via Radio Frequency Heating. *Carbon* **2021**, *182*, 564–570. [[CrossRef](#)]
26. Wang, L.; Wang, W.; Xu, G.; Ji, Z.; Lu, N.; Li, L.; Liu, M. Analytical Carrier Density and Quantum Capacitance for Graphene. *Appl. Phys. Lett.* **2016**, *108*, 013503. [[CrossRef](#)]
27. Liu, J.; Fan, L.; Su, J.; Yang, S.; Luo, H.; Shen, X.; Ding, F. Terahertz Time Domain Spectroscopic Response towards Different Macrocylic Antibiotics Using a One-Step Transfer Graphene Metamaterial Absorber. *Mater. Chem. Phys.* **2022**, *292*, 126784. [[CrossRef](#)]
28. Wang, X.; Wang, Y.; Yang, X.; Cao, Y. Numerical Simulation on the LSPR-Effective Core-Shell Copper/Graphene Nanofluids. *Sol. Energy* **2019**, *181*, 439–451. [[CrossRef](#)]
29. Park, M.J.; Choi, H.-H.; Park, B.; Lee, J.Y.; Lee, C.-H.; Choi, Y.S.; Kim, Y.; Yoo, J.M.; Lee, H.; Hong, B.H. Enhanced Chemical Reactivity of Graphene by Fermi Level Modulation. *Chem. Mater.* **2018**, *30*, 5602–5609. [[CrossRef](#)]
30. Yan, D.; Li, J. Tunable All-Graphene-Dielectric Single-Band Terahertz Wave Absorber. *J. Phys. D Appl. Phys.* **2019**, *52*, 275102. [[CrossRef](#)]
31. Zhu, X.; Wang, B. Graphene-Based Angle-Insensitive and Tunable Single-Band and Dual-Band Metamaterial Terahertz Absorber. *Phys. Status Solidi (b)* **2022**, *259*, 2100573. [[CrossRef](#)]
32. Lai, R.; Shi, P.; Yi, Z.; Li, H.; Yi, Y. Triple-Band Surface Plasmon Resonance Metamaterial Absorber Based on Open-Ended Prohibited Sign Type Monolayer Graphene. *Micromachines* **2023**, *14*, 953. [[CrossRef](#)] [[PubMed](#)]
33. Barnes, W.L.; Dereux, A.; Ebbesen, T.W. Surface Plasmon Subwavelength Optics. *Nature* **2003**, *424*, 824–830. [[CrossRef](#)] [[PubMed](#)]
34. Gao, S.Y.; Wei, K.H.; Yang, H.; Tang, Y.J.; Yi, Z.; Tang, C.J.; Tang, B.; Yi, Y.G.; Wu, P.H. Design of Surface Plasmon Resonance-Based D-Type Double Open-Loop Channels PCF for Temperature Sensing. *Sensors* **2023**, *23*, 7569. [[CrossRef](#)]
35. Meng, W.; Li, C.; Yao, M.; He, Z.; Wu, X.; Jiang, Z.; Dai, L.; Wang, L. Synthesis and electrochemical performance of Li_{1+x}Ti_{2-x}Fex(PO₄)₃/C anode for aqueous lithium ion battery. *Adv. Powder Technol.* **2020**, *31*, 1359–1364. [[CrossRef](#)]
36. Huang, C.; Ji, C.; Zhao, B.; Peng, J.; Yuan, L.; Luo, X. Multifunctional and Tunable Radar Absorber Based on Graphene-Integrated Active Metasurface. *Adv. Mater. Technol.* **2021**, *6*, 2001050. [[CrossRef](#)]
37. Mohsen Daraei, O.; Goudarzi, K.; Bemani, M. A Tunable Ultra-Broadband Terahertz Absorber Based on Two Layers of Graphene Ribbons. *Opt. Laser Technol.* **2020**, *122*, 105853. [[CrossRef](#)]

38. Zhu, Y.Y.; Cai, P.G.; Zhang, W.L.; Meng, T.Y.; Tang, Y.J.; Yi, Z.; Wei, K.H.; Li, G.F.; Tang, B.; Yi, Y.G. Ultra-Wideband High-Efficiency Solar Absorber and Thermal Emitter Based on Semiconductor InAs Microstructures. *Micromachines* **2023**, *14*, 1597. [[CrossRef](#)]
39. Nickpay, M.-R.; Danaie, M.; Shahzadi, A. A Triple-band Metamaterial Graphene-Based Absorber Using Rotated Split-Ring Resonators for THz Biomedical Sensing. *Opt. Quantum Electron.* **2023**, *55*, 193. [[CrossRef](#)]
40. Barzegar-Parizi, S.; Khavasi, A. Designing Dual-Band Absorbers by Graphene/Metallic Metasurfaces. *IEEE J. Quantum Electron.* **2019**, *55*, 1–8. [[CrossRef](#)]
41. Liu, W.; Liu, C.; Wang, J.X.; Lv, J.W.; Lv, Y.; Yang, L.; An, N.; Yi, Z.; Liu, Q.; Hu, C.J.; et al. Surface plasmon resonance sensor composed of microstructured optical fibers for monitoring of external and internal environments in biological and environmental sensing. *Results Phys.* **2023**, *47*, 106365. [[CrossRef](#)]
42. Shan, L.; Zhou, J.; Zhang, W.; Xia, C.; Guo, S.; Ma, X.; Fang, G.; Wu, X.; Liang, S. Highly Reversible Phase Transition Endows V_6O_{13} with Enhanced Performance as Aqueous Zinc-Ion Battery Cathode. *Energy Technol.* **2019**, *7*, 57. [[CrossRef](#)]
43. Rezagholizadeh, E.; Biabanifard, M.; Borzooei, S. Analytical Design of Tunable THz Refractive Index Sensor for TE and TM Modes Using Graphene Disks. *J. Phys. D Appl. Phys.* **2020**, *53*, 295107. [[CrossRef](#)]
44. Qin, F.; Chen, J.; Liu, J.W.; Liu, L.; Tang, C.J.; Tang, B.; Li, G.F.; Zeng, L.C.; Li, H.L.; Yi, Z. Design of high efficiency perovskite solar cells based on inorganic and organic undoped double hole layer. *Sol. Energy* **2023**, *262*, 111796. [[CrossRef](#)]
45. Lin, K.-T.; Lin, H.; Yang, T.; Jia, B. Structured Graphene Metamaterial Selective Absorbers for High Efficiency and Omnidirectional Solar Thermal Energy Conversion. *Nat. Commun.* **2020**, *11*, 1389. [[CrossRef](#)]
46. Wang, F.; Huang, S.; Li, L.; Chen, W.; Xie, Z. Dual-Band Tunable Perfect Metamaterial Absorber Based on Graphene. *Appl. Opt.* **2018**, *57*, 6916–6922. [[CrossRef](#)]
47. Zhu, L.; Hu, R.; Xiang, Y.; Yang, X.; Chen, Z.; Xiong, L.; Wu, X.; He, Z.; Lei, W. Enhanced performance of Li-S battery by constructing inner conductive network and outer adsorption layer sulfur-carbon composite. *Int. J. Energy Res.* **2020**, *45*, 6002–6014. [[CrossRef](#)]
48. Wu, X.; Li, Y.; Xiang, Y.; Liu, Z.; He, Z.; Wu, X.; Li, Y.; Xiong, L.; Li, C.; Chen, J. The electrochemical performance of aqueous re-chargeable battery of Zn/Na_{0.44}MnO₂ based on hybrid electrolyte. *J. Power Sources* **2016**, *336*, 35–39. [[CrossRef](#)]
49. Chen, H.; Li, W.; Zhu, S.; Hou, A.; Liu, T.; Xu, J.; Zhang, X.; Yi, Z.; Yi, Y.; Dai, B. Study on the Thermal Distribution Characteristics of a Molten Quartz Ceramic Surface under Quartz Lamp Radiation. *Micromachines* **2023**, *14*, 1231. [[CrossRef](#)]
50. Wu, X.W.; Li, Y.H.; Li, C.C.; He, Z.X.; Xiang, Y.H.; Xiong, L.Z.; Chen, D.; Yu, Y.; Sun, K.; He, Z.Q.; et al. The electrochemical performance improvement of LiMn₂O₄/Zn based on zinc foil as the current collector and thiourea as an electrolyte additive. *J. Power Sources* **2015**, *300*, 453–459. [[CrossRef](#)]
51. Wu, P.; Zeng, X.; Su, N.; Chen, M.; Zeng, Y.; Yu, Y. A Graphene Perfect Absorber with Tunable, Dual Band, High Sensitivity Characteristics. *Diam. Relat. Mater.* **2022**, *125*, 109002. [[CrossRef](#)]
52. Cheng, Y.; Zhu, X.; Li, J.; Chen, F.; Luo, H.; Wu, L. Terahertz Broadband Tunable Reflective Cross-Polarization Converter Based on Complementary Cross-Shaped Graphene Metasurface. *Phys. E Low-Dimens. Syst. Nanostructures* **2021**, *134*, 114893. [[CrossRef](#)]
53. Landy, N.I.; Sajuyigbe, S.; Mock, J.J.; Smith, D.R.; Padilla, W.J. Perfect Metamaterial Absorber. *Phys. Rev. Lett.* **2008**, *100*, 207402. [[CrossRef](#)] [[PubMed](#)]
54. Tralle, I.; Chotorlishvili, L.; Zięba, P. Explicit Fresnel Formulae for the Absorbing Double-Negative Metamaterials. *Phys. Lett. A* **2021**, *385*, 126963. [[CrossRef](#)]
55. Wu, X.; Li, Y.; Xiang, Y.; Liu, Z.; He, Z.; Wu, X.; Li, Y.; Xiong, L.; Li, C.; Chen, J. Mixed-valence cobalt oxides bifunctional electro-catalyst with rich oxygen vacancies for aqueous metal-air batteries. *Chem. Eng. J.* **2023**, *453*, 139831. [[CrossRef](#)]
56. Zheng, Y.; Yi, Z.; Liu, L.; Wu, X.W.; Liu, H.; Li, G.F.; Zeng, L.C.; Li, H.L.; Wu, P.H. Numerical simulation of efficient solar absorbers and thermal emitters based on multilayer nanodisk arrays. *Appl. Therm. Eng.* **2023**, *230*, 120841. [[CrossRef](#)]
57. Li, Y.; Yang, S.; Du, H.; Liu, Y.; Wu, X.; Yin, C.; Wang, D.; Wu, X.; He, Z.; Wu, X. A stable fluoride-based interphase for a long cycle Zn metal anode in an aqueous zinc ion battery. *J. Mater. Chem. A* **2022**, *10*, 14399–14410. [[CrossRef](#)]
58. Wu, X.; Tan, C.; He, C.; Zhao, T.; Wu, X.; Ma, Z.; Wang, H.; Cai, Y.; Wu, Q.; Li, Q. Strategy for boosting Co-Nx content for oxygen reduction reaction in aqueous metal-air batteries. *J. Power Sources* **2022**, *520*, 230891. [[CrossRef](#)]
59. Tang, F.; Wu, X.; Shen, Y.; Xiang, Y.; Wu, X.; Xiong, L.; Wu, X. The intercalation cathode materials of heterostructure MnS/MnO with dual ions defect embedded in N-doped carbon fibers for aqueous zinc ion batteries. *Energy Storage Mater.* **2022**, *52*, 180–188. [[CrossRef](#)]
60. Li, C.; Shi, X.; Liang, S.; Ma, X.; Han, M.; Wu, X.; Zhou, J. Spatially homogeneous copper foam as surface dendrite-free host for zinc metal anode. *Chem. Eng. J.* **2020**, *379*, 122248. [[CrossRef](#)]
61. Zhang, Y.; Pu, M.; Jin, J.; Lu, X.; Guo, Y.; Cai, J.; Zhang, F.; Ha, Y.; He, Q.; Xu, M.; et al. Crosstalk-free achromatic full Stokes imaging polarimetry metasurface enabled by polarization-dependent phase optimization. *Opto Electron. Adv.* **2022**, *5*, 220058. [[CrossRef](#)]
62. Zheng, Z.; Xu, L.; Huang, L.J.; Smirnova, D.; Kamali, K.Z.; Yousefi, A.; Deng, F.; Camacho-Morales, R.; Ying, C.; Miroshnichenko, A.E.; et al. Third-harmonic generation and imaging with resonant Si membrane metasurface. *Opto Electron. Adv.* **2023**, *6*, 220174. [[CrossRef](#)]
63. Kim, M.K.; Lee, D.S.; Yang, Y.H.; Rho, J.S. Switchable diurnal radiative cooling by doped VO₂. *Opto-Electron. Adv.* **2021**, *4*, 200006. [[CrossRef](#)]

64. Ye, Z.; Wu, P.; Wang, H.; Jiang, S.; Huang, M.; Lei, D.; Wu, F. Multimode tunable terahertz absorber based on a quarter graphene disk structure. *Results Phys.* **2023**, *48*, 106420. [[CrossRef](#)]
65. Zhou, W.; Qin, X.; Lv, M.; Qiu, L.; Chen, Z.; Zhang, F. Design of a New Type of In-Hole Gold-Coated High-Performance Quasi-PCF Sensor Enhanced with Surface Plasmon Resonance. *Coatings* **2023**, *13*, 1261. [[CrossRef](#)]
66. Veeraselvam, A.; Mohammed, G.N.A.; Savarimuthu, K. A Novel Ultra-Miniaturized Highly Sensitive Refractive Index-Based Terahertz Biosensor. *J. Light. Technol.* **2021**, *39*, 7281–7287. [[CrossRef](#)]
67. Khodadadi, B.; Babaeinik, M.; Ghods, V.; Rezaei, P. Triple-Band Metamaterial Perfect Absorber for Refractive Index Sensing in THz Frequency. *Opt. Quant. Electron.* **2023**, *55*, 431. [[CrossRef](#)]
68. Islam, M.S.; Sultana, J.; Biabanifard, M.; Vafapour, Z.; Nine, M.J.; Dinovitser, A.; Cordeiro, C.M.B.; Ng, B.W.-H.; Abbott, D. Tunable Localized Surface Plasmon Graphene Metasurface for Multiband Superabsorption and Terahertz Sensing. *Carbon* **2020**, *158*, 559–567. [[CrossRef](#)]

Disclaimer/Publisher’s Note: The statements, opinions and data contained in all publications are solely those of the individual author(s) and contributor(s) and not of MDPI and/or the editor(s). MDPI and/or the editor(s) disclaim responsibility for any injury to people or property resulting from any ideas, methods, instructions or products referred to in the content.